Combining Thickness Reduction and Light Trapping for Potential Efficiency Improvements in Perovskite Solar Cells

Marcos Soldera* and Kurt Taretto

In this contribution it is shown that the efficiency of perovskite solar cells based on $CH_3NH_3PbI_3$ can be increased further by combining thickness reduction of the perovskite layer and light trapping. A physical model for the current/voltage curve of *pin* solar cells is used to reveal the beneficial impact of thinning on cell efficiency. If interface recombination is kept at moderate levels, the model shows that there is a potential efficiency increase above 20% relative (+3% absolute) when thickness is reduced from 500 to 200 nm, provided total light absorption is maintained. A rigorous optical model is employed to calculate light absorption on typical state–of–the–art layer stacks patterned with sinusoidal grooves on ITO coated glass. The results suggest that solar light absorption in a flat, 500 nm thick film, can be matched by a 200 nm thick perovskite layer on a sinusoidal texture, while using 300 nm leads to several sinusoidal parameter combinations delivering the same light absorption. Since the structuring step must be compatible with low cost processing, it is shown that direct laser interference patterning (DLIP) is capable of delivering +3% absolute efficiency increase, while offering a typical photovoltaic module cost reduction of 10%.

1. Introduction

The fast and promising evolution of perovskite solar cells in terms of device efficiency and stability maintains a strong momentum within the scientific community working in low cost renewable energies. The ongoing improvements in device performance are obtained through the optimization of perovskite preparation recipes, investigation of optimum deposition conditions, role of electronic interfaces and functional layers, and degradation mitigation.[1–5] Up until recently, in this scenario of efficiency improvements through material and interface quality enhancement, optical optimization studies did not play a major role. Specifically, in solar cells based on the most widely spread photovoltaic perovskite $CH_3NH_3PbI_3$ (or MAPI),

optical optimization seems superfluous because MAPI shows an extremely sharp spectral absorption edge, being less than 1 µm thickness sufficient to completely absorb sunlight with photon energies above its bandgap. Evidently, an excellent combination of mobility and lifetime enables charge carriers to travel the whole thickness required for complete light absorption without major losses, yielding high efficiencies.[6] However, as the efficiencies of MAPI solar cells begin to lean out the 20% efficiency mark — reaching the range of state of the art silicon or thin film CdTe or $Cu(In,Ga)Se_2$ solar cells,[7] fine tuning of the cell stack with regard to optimum light absorption becomes meaningful. Thus, recently, also the optical optimization of the perovskite solar cell structure seen as an optical stack has attracted some attention.[8,9] Such strategies are aimed to optimize layer materials and thicknesses in the layer stack of perovskite solar cells, ultimately maximizing the cell's photocurrent.

Moreover, there is an additional, often overlooked, efficiency enhancement route that becomes accessible through optical optimization. Indeed, it can be shown by fundamental thermodynamical principles, that ideal *pn* cells show an increase in open–circuit voltage V_{OC} when thickness is reduced, provided total light absorption remains unchanged.[10] Notice that this implies that the fill factor FF also increases with thickness reduction, since in ideal *pn* solar cells FF increases monotonously with V_{OC}.[11] Notice also that under this efficiency improvement route, light trapping participates primarily to sustain the requisite of overall total light absorption at reduced thickness, rather than to improve the photocurrent at a given thickness. An additional requisite to enable improvements through thickness reduction is a low surface recombination at the interfaces of the absorbing layer.[10] Notably, the fulfillment of this requirement seems accessible in current MAPI solar cells, where low surface recombination velocities around or even below $10^3 \, cm \, s^{-1}$ have been recently reported by different authors.[6,12,13]

In order to confirm or reject the possibility to obtain concrete benefits of thickness reduction in the specific case of MAPI solar cells, in this work we model the electrical as well as the optical

Dr. M. Soldera, Prof. Dr. K. Taretto
PROBIEN, Departamento de Electrotecnia
CONICET–Universidad Nacional del Comahue
Neuquen 8300, Argentina
E-mail: marcos.soldera@fain.uncoma.edu.ar

The ORCID identification number(s) for the author(s) of this article can be found under https://doi.org/10.1002/pssa.201700906.

properties of MAPI solar cells with light trapping textures. Since current MAPI solar cells are most likely *pin* type junctions, the electrical model considers drift-diffusion physics in a *pin* solar cell. This analytical model poses a practical base to quantify the influence of thickness reduction on V_{OC}, *FF*, and device efficiency η, identifying conditions under which a thickness reduction enhances η. The optical model is then applied to find light trapping structures that would enable a thickness reduction maintaining the maximum available photocurrent, while at the same time being compatible with fast, low cost manufacturing line (see Section 3.3).

In the modeling section presented next, we apply the analytical *pin* solar cell model finding the electrical output parameters as the thickness of the intrinsic MAPI layer is varied. Next, we present the electromagnetic model for the optical numerical simulations and the employed geometries, showing their compatibility with large scale substrate structuring and smooth film growth. In the results section we show the dependence of maximum attainable photocurrents as a function of geometrical structure parameters, and find suitable combinations of these parameters to sustain photocurrent with decreasing thickness. We then discuss the implications of the found structures on series resistance of modules. Finally we give an outlook towards the benefits of the proposed approach in terms of power conversion efficiency enhancement and reduction of manufacturing cost per watt peak.

2. Electrical Model

2.1. Features and Assumptions

This section investigates the relation of solar cell output parameters with perovskite thickness, obtained by an analytical model for *pin* type solar cells[14] that was shown to deliver good agreement with experimental data.[6] Here, the intrinsic i-layer in the *pin* layer stack is the perovskite layer of thickness d_{pvk}, where we assume an intrinsic carrier concentration of $n_i = 6 \times 10^4$ cm^{-3},[6] a relative dielectric constant of $\epsilon_r = 33.5$,[45] and variable carrier mobilities and lifetimes, which are assumed equal for both electrons and holes, for simplicity. At the interfaces between the perovskite and the surrounding doped layers − here given by the hole and electron transport layers (HTL and ETL, respectively), the model assumes that minority carriers suffer a surface recombination velocity, assumed equal for both contact types. The difference in work functions between the HTL and ETL layers sandwiching the perovskite absorber determines the built–in voltage V_{bi} of the cell. Since for a given transport layer there is a range of possible work functions (depending on surface conditioning), we take an intermediate value of the difference in work functions. Adopting PCBM (lowest unoccupied molecular orbital between 3.8 to 4.3 eV[15,16]) as ETL and NiO (work function between 5.3 to 5.5 eV[17]) as HTL, we choose a moderate value for the work function difference by letting $V_{bi} = 1.2$ V. Regardless of the specific material choice, such work function differences are expectable also with other ETL and HTL layers for high efficiency MAPI solar cells. The minority carrier properties are assumed equal for electrons as well as holes. Both diffusion and drift transport are taken into account, where the drift obeys the electric

field in the i-layer, which is assumed homogeneous through the perovskite by $(V - V_0)/d_{pvk}$. Here, V is the externally applied voltage and V_0 a reduced built–in potential, which depends on the actual built–in voltage V_{bi} (see appendix). Regarding the photogeneration, for simplicity, the model considers a homogeneous photogeneration rate G across the active layer. The validity of this assumption depends on the thickness: if the thickness of the perovskite layer is below 300 nm, the photogeneration under AM1.5G illumination becomes oscillatory across the layer and varies by less than an order of magnitude between the maximum and minimum values. With smaller thickness the photogeneration rate becomes increasingly homogeneous due to the photons reflected at the back of the cell being absorbed in their second pass towards the front of the cell.[6] The error of assuming a constant generation rate also with higher absorber thickness was verified by numerical device simulations. We calculated solar cell output parameters using the simulator software PC1D[18] with 500 nm perovskite thickness, ideal contacts and the previously mentioned parameters, but including a position dependent photogeneration rate resulting from AM1.5G spectrum illumination instead of a constant photogeneration rate. The simulations delivered, at the same short–circuit current, an 8% lower open–circuit voltage in the cell simulated with the position dependent photogeneration rate. The discrepancy drops to below 3% difference at 300 nm thickness, which reinforces our results in the region of interest of this work.

In the appendix we display the mathematical expressions corresponding to the *pin* model, along with the analytical current/voltage equation. When fitting experimental *I(V)* curves of solar cells, it is important to notice that this model shows a voltage–dependent photocurrent as well as a voltage–dependent saturation current.[6] This enables obtaining physically more meaningful and accurate fits than those delivered by a one–diode model, but on the other hand simple relationships between for example V_{OC} and d_{pvk} are not accessible. Therefore, the model employed here serves to obtain analytic curves of the output characteristics of perovskite solar cells with decreasing thickness, with a minimum number of physical material parameters. In order to maintain the condition of constant maximum available photocurrent $J_{photo,max}$, the adopted photogeneration rate is varied with thickness according to $G = J_{photo,max}/qd_{pvk}$. In practice, this condition would only be achievable with increasing light trapping when the thickness decreases; the conditions to reach such light trapping are obtained within the optical model presented in the next section.

2.2. Modeling Results

Figure 1 shows the resulting output parameters: efficiency η, short–circuit current density J_{SC}, open–circuit voltage V_{OC}, and fill–factor *FF*, as a function of the perovskite thickness d_{pvk}. The maximum photocurrent density was assumed at $J_{photo,max} = 22$ mA cm^{-2}, matching current experimental data of efficient cells,[19–21] and the sunlight absorption of the particular layer stack employed in this work (see below), assuming perfect carrier collection (or unity internal quantum efficiency). These calculations use material parameters obtained from previous analyses by different methods,[6,22–24] yielding: bulk lifetime
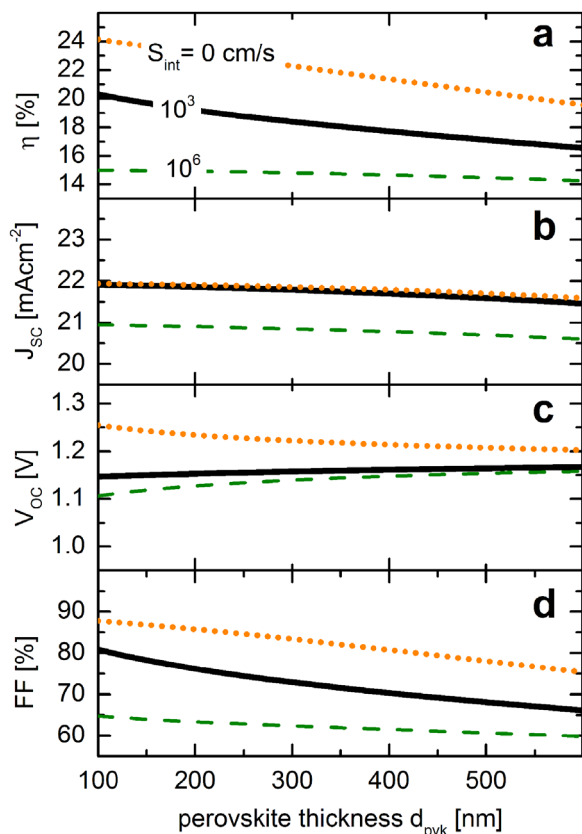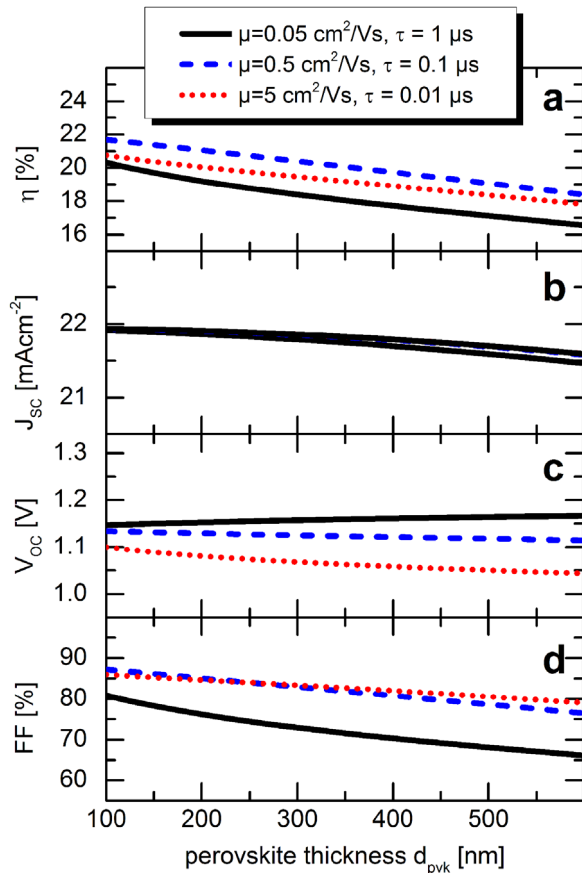
Figure 1. Modeled conversion efficiency η, short circuit current density J_{SC}, open–circuit voltage V_{OC} and fill factor FF for a thin film *pin* solar cell as a function of perovskite thickness d_{pvk}. The parameters are calculated with three recombination velocities S_{int} at the interface of the i-layer. The maximum available photocurrent is kept constant at 22 mA cm^{-2}. With decreasing thickness, J_{SC} and FF increase, regardless of S_{int}, while V_{OC} increases only at extremely low interface recombination velocities.

$\tau = 1\,\mu s$, mobility $\mu = 0.05\,cm^2\,V^{-1}\,s^{-1}$ (see below for analyses using different values). Overall, we see that the efficiency increases when the perovskite thickness decreases. As a parameter we adopted the interface recombination velocity S_{int} (see Figure 1), which is the quantity that should ideally be negligible in order to maximize the benefits of thickness reduction, here reflected by the curve with $S_{int} = 0$ (dotted line). Interestingly, Figure 1a shows that the efficiency increases even at high $S_{int} = 10^6\,cm\,s^{-1}$ (dashed line), and with an intermediate interface recombination, $S_{int} = 10^3\,cm\,s^{-1}$ (solid line), the efficiency increases by more than 20% relative ($\Delta\eta = +3.3\%$ absolute) when reducing the thickness from $d_{pvk} = 600\,nm$ to $d_{pvk} = 100\,nm$. A more modest reduction of thickness, from 500 to 200 nm, still yields a 12% relative efficiency increase ($\Delta\eta = +2\%$ absolute). Notice that the main contribution to the efficiency increase stems from the fill factor FF (Figure 1d), which for the intermediate case with $S_{int} = 10^3\,cm\,s^{-1}$ shows a 20% relative increase in the studied thickness range (see below for details). Since several reports point to an inherently low interface recombination velocity in $CH_3NH_3PbI_3$ perovskites,[6,12,13] the benefit of thickness reduction seen in Figure 1 seems a feasible improvement path in solar cell optimization.

Let us deepen our interpretation of the results. Figure 1b shows the increase of the short–circuit current density, which with decreasing d_{pvk} occurs regardless of interface recombination. This originates from the increasing collection probability of photogenerated carriers, not only because of the smaller thickness at equal lifetime and mobility, but also as a special feature of the *pin* solar cell, since the electric field increases when reducing d_{pvk}. Regarding the open–circuit voltage (Figure 1c), we notice that the chosen interface recombination velocities lead to three different behaviors: the highest $S_{int} = 10^6\,cm\,s^{-1}$ yields a decrease in V_{OC} of 50 mV when reducing d_{pvk} from 600 to 100 nm, $S_{int} = 10^3\,cm\,s^{-1}$ behaves neutrally, and the curve with $S_{int} = 0$ shows an increase in V_{OC} of 50 mV (see dotted line in Figure 1c). For comparison, the case with $S_{int} = 0$ agrees with the thermodynamic prediction for an ideal *pn* junction, where $\Delta V_{OC} = -V_t\Delta d_{pvk}/d_{pvk}$.[10] Indeed, with a thermal voltage of $V_t = 25\,mV$, centering the discrete derivative around $d_{pvk} = 250\,nm$ and taking $\Delta d_{pvk} = +500\,nm$, we obtain $\Delta V_{OC} = -50\,mV$, agreeing with our model. The fill–factor FF contributes the most to the efficiency boost, showing a steady increase with decreasing thickness (Figure 1d). Our calculations show that the increase comes from both, a higher photocurrent at the maximum power point (not shown in Figure 1), and an almost equally higher maximum power point voltage (except when $S_{int} = 10^6\,cm\,s^{-1}$). It can be understood from thermodynamical considerations, that the higher voltage originates from an increased photocarrier concentration in the thinner cells,[10] while the higher photocurrent is due to superior photocarrier collection in thinner samples where the electric field is stronger. This is again a consequence of the working principle of the *pin* structure, contrasting with the traditional view of ideal *pn* junction solar cells, where FF depends only on V_{OC}.[11]

We are aware of the fact that the results shown here depend on the specific material parameters, which are currently much under debate. Although the choice of the values of V_{bi}, τ and μ adopted in the results in Figure 1 correspond to $J(V)$ curve fitting of experimental results in state of the art devices (discussed in detail in Ref. [6]), here we show further calculations varying two orders of magnitude in μ and τ, but keeping $\mu\tau = 5 \times 10^{-8}\,cm^2\,V^{-1}$, which is the same as in the calculations shown in Figure 1. The curves in **Figure 2** are calculated using μ and τ values indicated in the inset, and $S_{int} = 10^3\,cm\,s^{-1}$ (thus, the solid line in Figure 2 is the same as in Figure 1). Let us mention that perhaps one of the less known parameters in perovskite solar cells is the built–in voltage. When calculating the output parameters with $\pm 0.1\,V$ different built–in voltages, we again obtain efficiency enhancements towards thinner cells, which are highly similar to the results of Figure 2.

Figure 2 shows that taking $\Delta d_{pvk} = -500\,nm$ as from 600 to 100 nm, the enhancement in efficiency is $\Delta\eta > 3\%$ absolute ($\Delta\eta = 2\%$ when $\Delta d_{pvk} = -300\,nm$), regardless of the combination of μ and τ. This result is not trivial, since the model depends on the one hand on the product $\mu\tau$ (see Eq. (9) in the appendix), and, independently, on the mobility μ, Eq. (11). The highest efficiency is obtained with intermediate μ and τ values, which is a consequence of the balance between bulk and interface recombination.[25] This balance can be understood rationalizing the influence of different μ and τ combinations on the open–circuit voltage (Figure 2c). Although the interface recombination is the same in all three cases, we again obtain decrease/increase/

Figure 2. Modeled conversion efficiency η, short circuit current density J_{SC}, open–circuit voltage V_{OC} and fill factor FF for a thin film *pin* solar cell as a function of perovskite thickness d_{pvk}. The parameters are calculated with three sets of carrier mobility μ and lifetime τ, maintaining the product $\mu\tau$. Although all three sets profit similarly from thickness reduction, the highest efficiency is obtained at intermediate μ and τ. The calculations keep a constant value of the interface recombination velocity $S_{int} = 10^3\,\mathrm{cm\,s}^{-1}$ and the maximum available photocurrent of 22 mAcm^{-2}.

neutral behaviors of V_{OC} with decreasing thickness. The increase is achieved in the case with the highest μ, because if bulk lifetime is low and interface recombination velocity moderate, the highly mobile carriers are able to reach the interfaces and benefit from a lower interface recombination. Thinning the absorber allows increasingly more carriers to reach and recombine at the interfaces, yielding the behavior seen on the dashed curve of Figure 2c. Conversely, low mobility in a bulk with high bulk lifetime yields higher absolute V_{OC} values, but as the thickness is reduced, more carriers reach the surface, losing the profit of high bulk lifetime (Figure 2c, solid curve). As a result of these trends, the highest efficiency is obtained with intermediate μ and τ values (Figure 2a, dashed curve). This result has been studied in detail in organic bulk heterojunction solar cells, where optimum mobilities for different recombination parameters can be found.[25]

The improvements of using thinner absorber layers obtained with the electrical model rely on maintaining the maximum photocurrent. In the next section, we show the simulation results

obtained with the optical model, which let us identify possible geometries that could sustain a high maximum photocurrent as thickness is reduced.

3. Optical Simulations

3.1. Device Structure and Model Setup

The simulated layer stack shown in **Figure 3**a is composed of a sodalime glass superstrate, a transparent front contact made of the transparent conductive oxide (TCO) indium tin oxide (ITO), NiO as HTL, the absorber layer is the perovskite CH$_3$NH$_3$PbI$_3$, PCBM as ETL, and finally silver is used as rear contact. The optical properties of these materials were taken from the Ref. [26–28]. The sketch in Figure 3a indicates also the thickness of each layer. In order to obtain an accurate description of the light propagation and absorption within each layer of the cell
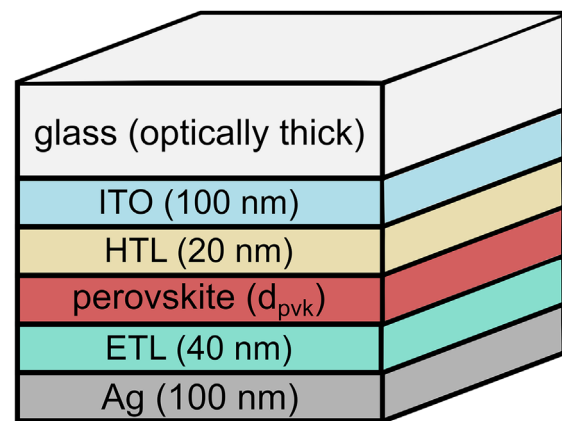
(a)
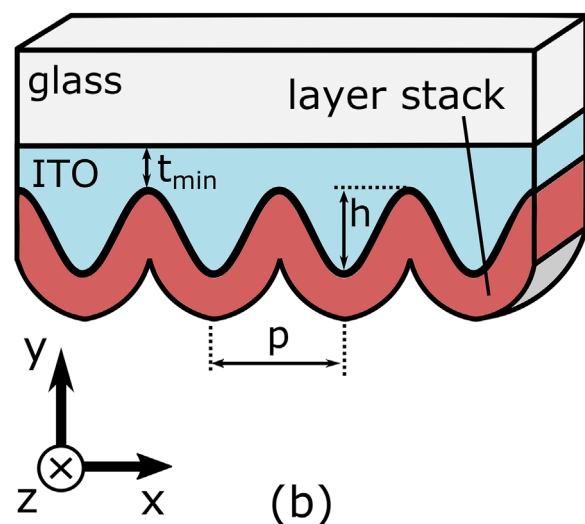
(b)

Figure 3. Schematic representation of the (a) simulated layer stack (see text for details) and layer thicknesses, and (b) the modeled sinusoidal, one dimensional texture with its optimization parameters.

stack, Maxwell's equations must be solved rigorously using the finite element method (FEM) to obtain the three-component steady state electric field, which is represented by complex values.[29]

Our simulations are aimed to enhance light absorption in the semiconductor by the interaction of light with periodical patterns realized on the front electrode, forming a textured electrode surface. We restrict the geometrical textures to those achievable by direct laser interference patterning (DLIP), a method based on the overlap of two or more pulsed laser beams with different optical paths. An interference pattern is obtained on the sample, where at the maximum intensity positions the material is ablated while at the minima the material remains nearly unaffected. This method meets industrial standards such as high processing speeds (1–$5\,\mathrm{m^2\,min^{-1}}$), single step processing since it does not require pre– or post-manufacturing steps, and it does not produce significant amounts of hazardous waste.[30,31] Among the vast variety of pattern shapes that can be fabricated with DLIP, the periodic 1D sinusoidal groove, shown in Figure 3b, offers the advantages of high simplicity and low processing time, while for the purpose of simulation, the least computational effort and computing time. Figure 3b shows schematically the texture parameters, namely the sine period p and height h and the minimum ITO thickness $t_{\min}$. The period was swept between $p = 0.3\,\mu\mathrm{m}$ and $p = 3\,\mu\mathrm{m}$, while the height was varied from $h = 100\,\mathrm{nm}$ to $h = 500\,\mathrm{nm}$. Although the simulations shown here were done with a fixed $t_{\min} = 100\,\mathrm{nm}$, below we discuss the impact of $t_{\min}$ on the lateral resistance of ITO. Notice that the combination of the period and height values yields aspect ratios $AR = h/p$, from $AR \approx 0.03$ to $AR \approx 1.7$. In the text below, the possibilities and limitations to produce such textures by DLIP are discussed.

We assume that conformal growth of the perovskite layer on the textured ITO substrates corresponds to an idealization that can be only physically feasible on low aspect ratio substrates, for example $AR < 0.1$, or for very thin perovskite films, for example. $d < 100\,\mathrm{nm}$. Consequently, in all the simulated geometries we have used a non-conformal growth model[32] based on the principle of isotropic growth, where at any point over the underlying surface the layer grows along the normal direction of the surface. At low aspect ratios and for thin layers this model yields the same layer profile as the conformal growth. Despite insufficient experimental analyses of perovskite growth on micro/nano textured substrates are available in the literature, we consider that this growth model is a far better approximation to the real case than the ideal conformal growth model. Additionally, the isotropic growth model yields constant thickness in the surface's normal direction, implying a uniform mean electric field along the surface normal. The uniform field enables a straightforward consistency with the analytical drift–diffusion model for flat cells introduced above.

To obtain a standardized photocurrent the simulations assume an incoming AM1.5G $100\,\mathrm{mW\,cm^{-2}}$ spectrum in the wavelength range from 300 to 850 nm. Longer wavelengths are neglected since the perovskite does not absorb them significantly. Since the solar radiation is essentially non-polarized,[15] the solar spectrum is split into two components with the same electromagnetic energy, namely a transverse electric mode (TE) with the electric field along the groove direction, and a transverse

magnetic mode (TM) with the magnetic field along the groove direction. Then the results are averaged for each simulation step.

Notice that the glass substrate is the only material in the stack that has a thickness much larger than the simulated wavelengths and therefore incoming light must be treated incoherently in this subdomain. Among the several approaches to address this issue,[33–35] we implement in our model the phase elimination method,[33] which has the advantage of requiring only two simulation runs to accurately model the incoherent propagation of light in the substrate and the coherent propagation in the rest of the layer stack. On top of the air domain, a perfectly matched layer (PML) with the same refractive index as air is defined for the purpose of absorbing all outgoing radiation and avoiding subsequent re-entering of spurious reflected light.[36] The lateral boundary conditions are assumed periodic to account for diffraction of incoming light.

Once the electric field vector $\boldsymbol{E}$ is obtained, the average electromagnetic energy density absorbed in a material with complex index of refraction $\tilde{n}(\lambda) = n(\lambda) + i\kappa(\lambda)$ is defined as[37]

$$Q(x, y, \lambda) = \frac{1}{2}c\varepsilon_0 n(\lambda)a(\lambda)|E(x, y, \lambda)|^2, \tag{1}$$

where λ is the free space wavelength of the plane electromagnetic wave, c is the speed of light in vacuum, ε_0 is the permittivity of free space, and a is the absorption coefficient defined as $a = 4\pi\kappa(\lambda)/\lambda$. The free carrier photogeneration rate is proportional to the energy absorbed in the perovskite layer according to

$$G(x, y, \lambda) = Q_{perovskite}(x, y, \lambda)/(hc/\lambda), \tag{2}$$

where h is Planck's constant. Finally, in short circuit conditions we consider that all the photogenerated carriers are extracted through the contacts of the solar cell. This implies that the maximum available photocurrent density is given by the integral of the photogeneration rate in the volume and over the simulated spectrum, according to
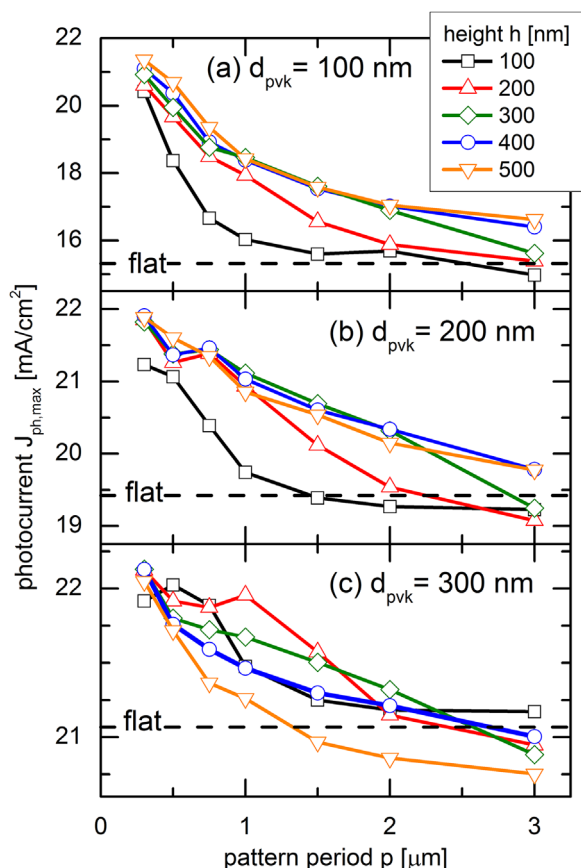
$$J_{\mathrm{ph,max}} = q\int_{300\mathrm{nm}}^{850\mathrm{nm}}\int_V G\,dV\,d\lambda/S, \tag{3}$$

where q is the elementary charge and S is the projected solar cell area in the substrate plane.

The electromagnetic model is implemented with the software COMSOL Multiphysics. For a detailed description of the electromagnetic model and its implementation in COMSOL see Ref. [38]. The mesh is generated by COMSOL using triangular elements with the constraint that the minimum effective wavelength is at least five times larger than the element size in each subdomain.[29] With this consideration, typical mesh sizes range from 20 000 to 70 000 elements, depending on the geometry parameters.

3.2. Numerical Simulation Results

Figure 4 shows the calculated maximum photocurrent $J_{\mathrm{ph,max}}$ of structured solar cells with a perovskite layer as defined from the

ADVANCED
SCIENCE NEWS
www.advancedsciencenews.com

physica
pss
status solidi
a

www.pss-a.com

Figure 4. Calculated maximum photocurrent as a function of the sinusoidal groove period p and height h. Three different perovskite thicknesses d_{pvk} were tested, (a) 100 nm, (b) 200 nm, and (c) 300 nm. Dashed lines show the photocurrent of flat devices with the same perovskite thickness.

isotropic growth model described previously, having the thickness d_{pvk}: (a) 100 nm, (b) 200 nm, and (c) 300 nm, with the pattern period p and height h as parameters. For comparison, we include the maximum photocurrent calculated for the corresponding flat perovskite solar cells (dashed horizontal lines) with the same absorber thickness. In the three subfigures we observe two general trends: highest $J_{ph,max}$ are obtained either with shorter periods p, or larger groove heights h. A notable exception occurs in the specific range of periods between $p = 0.5\,\mu m$ and $p = 1.5\,\mu m$, when $d_{pvk} = 300$ nm (Figure 4c), which shows that the highest photocurrents are obtained at the lowest pattern heights, that is $h = 100$ nm and $h = 200$ nm. In the case of cells with $d_{pvk} = 100$ nm (Figure 4a) the maximum relative increase in $J_{ph,max}$ compared to the flat device with the same thickness can be as high as 39%. When the perovskite thickness is increased to 200 nm (Figure 4b), the relative maximum photocurrent enhancement is 13%, while in the case of the 300 nm thick perovskite (Figure 4c), the relative increase is only 5%. As the absorber thickness increases further the photocurrent enhancement relative to the flat device continues to drop (not shown in Figure 4) and for $d_{pvk} = 500$ nm the increase is negligible.

As we have discussed in previous contributions, it is expected that the patterns with periods comparable to the wavelength of incoming light promote the diffraction of light into multiple modes that travel within the semiconductor along oblique directions.[38,39] This yields an enhancement in the optical path inside the perovskite and therefore an increase in the absorption and maximum photocurrent. The textures with periods larger than the simulated wavelengths, that is $p > 1.5\,\mu m$, can still benefit from two optical phenomena, namely the refraction of light at the TCO/HTL interface with the following oblique propagation of light within the semiconductor, and the increased absorption probability caused by multiple reflections of light between adjacent facets of the pattern. However, as can be deduced from the rather poor photocurrent increase for periods larger than 1.5 µm seen in Figure 4, these effects appear to be hardly beneficial for solar cell performance. We also see that in some cases the textured solar cells deliver even less photocurrent than the corresponding flat device, which is due to increased parasitic light absorption (see discussion below).

Figure 5 gathers the absolute maximum photocurrents (closed symbols) of the structured devices of Figure 4 for each simulated pattern period p and absorber thickness d_{pvk}. It is worth noting that state of the art DLIP technology cannot be used to fabricate textures with aspect ratios higher than $AR = 0.4$ on oxides. Therefore, we show in Figure 5 with open symbols the photocurrent obtained from devices where $AR < 0.4$, which are therefore compatible with current DLIP technology. Dashed lines in Figure 5 correspond to the photocurrent delivered by flat solar cells with the indicated perovskite thickness. Notice that at 600 nm thickness, the photocurrent of the flat devices nearly saturates at its maximum possible value for a flat cell with the chosen layer sequence (calculated at 22.5 mA cm^{-2} at infinite thickness, not shown in Figure 5–right). Since in this work we are interested in the benefits of light trapping upon thickness reduction, Figure 5 is better understood choosing a desired value of $J_{ph,max}$ and comparing the required thickness for the structured versus flat device, obtaining the allottable thickness reduction. For example, the value of $J_{ph,max}$ corresponding to a flat, 500 nm thick cell, can be obtained with structured solar cells with $d_{pvk} = 300$ nm down to $d_{pvk} = 200$ nm (simulation data above the flat 500 nm line in Figure 5). Also, these results should be compatible with DLIP–processing compatible structures ($AR < 0.4$, open symbols). This example suggests that upon structuring, the photocurrent can be maintained when the thickness decreases by a factor between 2 and 3 (depending on the geometrical parameters). The enhancements in efficiency $\Delta\eta$ of thinning the absorber from 500 to 200 nm were discussed above for perovskite *pin* cells, being $\Delta\eta = 2$ to 3% —above a flat 500–600 nm thick solar cell— possible at moderate interface recombination velocities. In practice, special care should be laid on the deposition of the HTL, perovskite and ETL on the textured substrates, since the interface quality can play a major role in the performance. In addition to the fundamental physical benefits, thickness reduction enables cost reduction through reduced material usage, and therefore compensates in part the cost of using thicker TCO substrates.
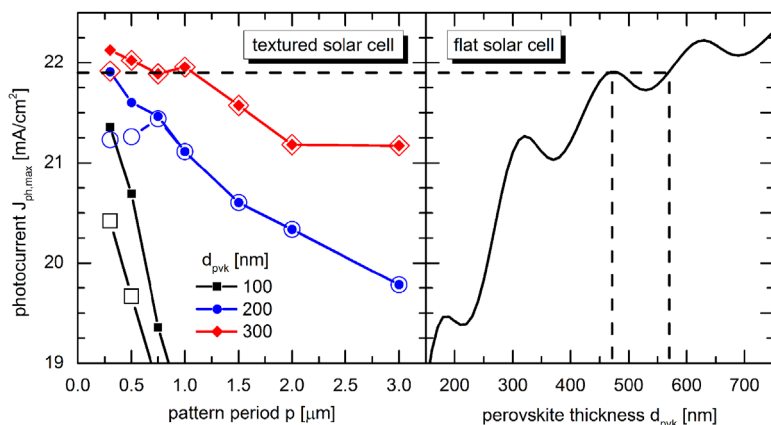
Figure 5. The left plot shows with closed symbols the absolute maximum photocurrent calculated for the textured solar cells for each simulated period and with open symbols the maximum photocurrent calculated for textured devices, whose pattern has an aspect ratio lower than 0.4. The right plot indicates the maximum photocurrent delivered by flat solar cells as a function of the perovskite thickness.

Let us proceed to a spectral analysis of light absorption and photogeneration. As a general trend, we have observed that the gain in photocurrent upon using structured substrates corresponds with a decrease in reflectance over the whole simulated spectrum, with a stronger impact in the 600–750 nm wavelength range. A deeper insight into the optical losses is possible with **Figure 6**, showing the reflectance R, absorbance A of the perovskite, and the parasitic absorbance in the (a) flat solar cell and (b) structured device with $p = 750$ nm and $h = 200$ nm. In both cases $d_{pvk} = 200$ nm. The numbers next to the R and $A_{parasitic}$ labels in the graph point out the current losses associated to the reflectance or parasitic absorption, respectively.
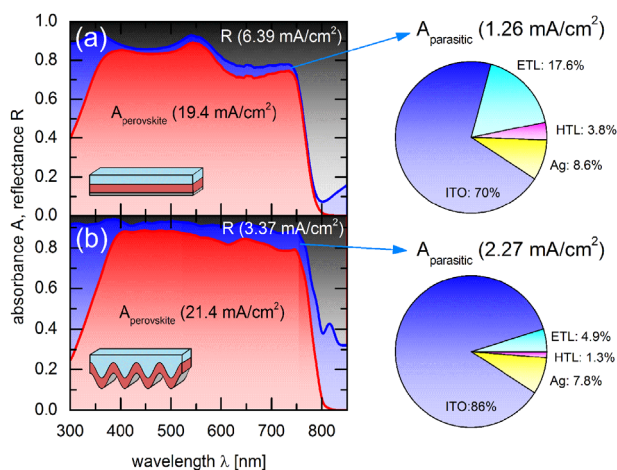
Figure 6. Absorbance of the perovskite layer, contact layers (parasitic) and reflectance R for the (a) flat device and (b) patterned device with texture parameters $p = 750$ nm and $h = 200$ nm. In both cases the perovskite layer is 200 nm thick. The numbers in brackets indicate the photocurrent (next to the perovskite), and the photocurrent losses due to parasitic absorption and reflectance, respectively. The pie charts show the contribution of each contact layer to the parasitic absorbance loss.

Next to the $A_{perovskite}$ label it is shown the calculated $J_{ph,max}$. The periodic pattern on the substrate clearly reduces the reflectance in the whole studied wavelength range, especially in the red-near infrared spectrum. Nonetheless, this reduction of reflected light does not correlate straightforward to the photocurrent enhancement, since the parasitic absorption increases after structuring too. Quantitatively, the photocurrent loss due to reflected light is decreased by 3 mA cm^{-2} upon structuring, while the current loss associated to parasitic absorption increases 1 mA cm^{-2} and therefore the photocurrent increases 2 mA cm^{-2}. As shown in the pie charts in Figure 6, the current loss due to absorption in ITO surpasses the combined losses in the rest of the contact layers in the flat device as well as in the structured one. Notice also that in the structured device the contribution of the absorption in ITO in the photocurrent loss is more pronounced than in the flat device. Consequently, further efforts to reduce optical losses in these devices should be aimed at reducing the absorption in the front contact, by means of optimizing its thickness or by replacing it with a more transparent material with similar electrical characteristics.

Experimental work needs to be done to verify our hypotheses and validate the calculated efficiency enhancements of MAPI solar cells on DLIP structured substrates. This task can become challenging due to the multiple factors that can affect the films formation upon growing on patterned substrates. For the sake of simplicity, the simulations shown here assume that the electronic quality of the interfaces and in the perovskite bulk does not deteriorate significantly when using these laser structured substrates instead of the flat TCO coated glass. Despite there has not been reported a significant amount of experimental perovskite solar cells on textured substrates yet, recent experimental results hint to the validity of this assumption. On the one hand, MAPI solar cells fabricated on randomly structured FTO coated substrates delivered a 14.5% increase in short-circuit current compared to a reference device,[40] and on the other hand, MAPI solar cells prepared on periodic inverted nanocones yielded a photocurrent increase of 38% relative to the flat device.[41] In both cases the enhanced photocurrents, and device efficiencies, were attributed to an effective light trapping effect. Both results suggest a negligible deterioration of material parameters of the perovskite deposited on structured substrates. At least in the case of the randomly textured cell,[40] where the open-circuit voltage remained equal, recombination parameters cannot have deteriorated. On another note, organic and a-Si:H/μc-Si:H tandem solar cells have been prepared on DLIP processed substrates, showing photocurrents and efficiencies enhanced by 9–21%.[42–44] Since the values of FF and V_{OC} remained nearly unchanged compared to reference devices, we can, on the one hand, discard a noteworthy decrease of shunt resistance in the structured solar cells, and on the other hand, suggest that the patterning on the TCO does not modify significantly the surface recombination velocity of the active layers. Nevertheless, these observations must still be proven on perovskite solar cells deposited on DLIP patterned substrates to test our model.

**ADVANCED
SCIENCE NEWS**

www.advancedsciencenews.com

p s s a
physica status solidi

www.pss-a.com

3.3. Cost Analysis Including DLIP

Since the structuring process implies higher fabrication costs, here we estimate the potential impact of the addition of DLIP processing step on the total perovskite photovoltaic module manufacturing costs. To cover a broad spectrum of possible mass production alternatives, we follow three cost analysis models for perovskite modules which consider different contact materials, deposition technologies and device configurations. Model I is based on the analysis reported in Ref. [45] for *pin* perovskite modules which proposes the use of low cost contact materials such as screen printed NiO and ZnO and low temperature processes. Model II represents the cost analysis corresponding to the sequence C presented in Ref. [46], where the *nip* perovskite module is fabricated with high temperature processes such as sintering and metal thermal evaporation, and the expensive P3HT is used as hole transport layer. Finally, model III stands for the sequence L1 of Ref. [46] which represents a limiting situation of the model II where the costs of processing the active layers and back contact turn negligible. According to Ref. [47] the DLIP manufacturing cost in 2015 was approximately $3.62\,\$\,m^{-2}$ for processing TCO materials taking into account one operator working 52 weeks, 39 h a week with 100% overhead and the cost necessary for acquiring the equipment distributed in 3 years at maximum fabrication speed. Based on these assumptions we envisage two distinct scenarios, which we define as pessimistic and optimistic. Within the pessimistic scenario we suppose that DLIP technology is already mature and its processing costs would not decrease further from the last reported value of $3.62\,\$\,m^{-2}$. Additionally, in this scenario we assume a sub-standard DLIP versatility, capable of delivering only sub-optimum textures that imply an efficiency boost of only 1.5% absolute. Turning to the optimistic scenario, we expect that further development of DLIP technology sinks the manufacturing costs to $1.8\,\$\,m^{-2}$, and the module efficiency gain through light trapping can readily reach our calculated value of 3% absolute.

Naturally, since the initial, that is prior to DLIP processing, module efficiency is critical for the correct estimation of final costs, we propose two reasonably module efficiencies as a starting point, namely 14 and 18%. The cost calculation results are shown in **Table 1**, which summarizes the estimated reduction in module costs in American dollars per watt peak ($/Wp) after the efficiency improvement through DLIP processing according to the three proposed models and under the two envisioned scenarios. We observe that the estimated module costs can be significantly reduced upon structuring with

DLIP reaching a maximum saving of 15%. In the worst case scenario the cost reduction drops to 1–5%, but it still could imply a meaningful enhancement towards lowering the cost of perovskite photovoltaics.

Current DLIP technology can achieve a manufacturing throughput of $0.5–1\,m^2\,min^{-1}$[47] on TCO substrates, and therefore it could imply an increase in the module processing time from 0.7–2 to $1.2–3\,min\,m^{-2}$.[45,46] It is expected that the ongoing development of DLIP technology should continue to reduce the processing time and costs in the short term, making this technology even more suitable for low cost photovoltaics.

3.4. A Note on Electrical Resistance Losses

In non-structured (i.e., flat) solar cells, the TCO thickness is chosen as an optimum thickness that balances parasitic light absorption, series resistance, and manufacturing and material costs. Since several TCO structuring methods are subtractive, meaning the final effective TCO thickness is smaller than the initial thickness, it is straightforward to realize that in structured solar cells, the optimum initial TCO thickness shifts to a different position depending on the desired final texture. If we depart from a substrate with a TCO thickness optimized for a flat solar cell, after structuring the resulting series resistance of the cell will be higher, yielding a lower fill factor and a decreased efficiency. In order to minimize fill factor losses due to series resistance, one could choose a higher initial TCO thickness, or, accept a limited resistance increase with negligible impact on fill factor. Here, we ponder the impact of structuring on resistance in terms of the effective TCO thickness after structuring. It is straightforward to calculate the effective thickness t_{eff} required to obtain a given TCO layer resistance R_{TCO} in a sinusoidally structured TCO with pattern height h (i.e., sine amplitude of $h/2$) and minimum thickness $t_{\min}$ (cf. Figure 3b), which yields $t_{\mathrm{eff}} = \sqrt{t_{\min}(h + t_{\min})}$. For example, setting $t_{\min} = 100\,nm$ and $h = 200\,nm$, making $t = h + t_{\min} = 300\,nm$ total TCO thickness before subtractive structuring, we obtain $t_{\mathrm{eff}} = 173\,nm$. This means that, compared with a flat, 300 nm thick TCO, this choice of structuring parameters implies an increase in layer resistance by a factor $300/173 = 1.73$. Conversely, we can establish a desired R_{TCO} and find out the required initial TCO thickness by solving the equation above, which yields

$$t = h/2 + \sqrt{(h/2)^2 + t_{\mathrm{eff}}^2}. \tag{4}$$

Table 1. Estimated module cost after the DLIP processing step considering three cost analysis models (described in the text). Two possible scenarios are proposed: in the pessimistic one the DLIP processing cost is $3.62\,\$\,m^{-2}$ and the efficiency boost by light trapping is 1.5% absolute, while in the optimistic one the DLIP technology cost is reduced to $1.8\,\$\,m^{-2}$ and the efficiency gain climbs up to 3% absolute.

				Pessimistic scenario			Optimistic scenario		
	Initial module cost [$/Wp]			Relative cost variation [%]			Relative cost variation [%]		
Initial efficiency η [%]	Model I	Model II	Model III	Model I	Model II	Model III	Model I	Model II	Model III
14	0.47	–	0.39	−4.7	–	−3.7	−15.4	–	−14.9
18	0.37	0.7	0.29	−2.7	−5.0	−1.3	−12.0	−13.0	−11.3

For example, if R_{TCO} should correspond to a planar TCO thickness $t_{eff} = 150$ nm, a light trapping structure with $h = 200$ nm must have an initial TCO thickness $t = 280$ nm (implying $t_{min} = 80$ nm). Aiming at a specific value of R_{TCO} effectively imposes a restriction on the optical optimization procedure. The light trapping structure should be optimized for maximum photocurrent in terms of h and period p with the restriction that for a chosen h, the total thickness t must obey Eq. (4), assuming that the laser processing does not modify the resistivity of the material.

4. Conclusions

This contribution investigates the potential efficiency improvement of $CH_3NH_3PbI_3$ based solar cells through a combination of perovskite thickness reduction and light trapping. It is found that the fill factor impacts the most on the efficiency boost obtained by thinning plus light trapping. The modeling results show that there is a potential 20% relative (3% absolute) efficiency increase in solar cells prepared with $CH_3NH_3PbI_3$ with state–of–the–art physical transport and recombination parameters when reducing the perovskite thickness from 500 to 200 nm. The requirements to access this efficiency boost are a good level of light trapping and interface recombination velocities not much higher than 1000 cm s^{-1}, which seems feasible in view of recent experimental evidence.[12] Detailed optical simulations at AM1.5G spectrum illumination show that the required level of light trapping must not be necessarily extreme: sine–shaped patterned ITO substrates with structure periods and pattern heights below 1 and 0.3 μm, respectively, with a 200 nm thick perovskite layer, are sufficient to achieve nearly the same light absorption as in a flat, 500 nm thick perovskite absorber. The proposed textured ITO is readily achievable with industrial–grade direct laser interference patterning,[30,47] suggesting a practical route to enhance module efficiency on optimized devices and reducing the final manufacturing costs per watt peak. In order to obtain experimental data on the possibilities of light trapping in perovskites, first experiments on light absorption in perovskites deposited on DLIP structured ITO substrates are currently undertaken in our laboratory.

Conflict of Interest

The authors declare no conflict of interest.

Appendix

The analytical drift-diffusion model of Ref. [6] assumes negligible photovoltaic contribution of the doped layers, only the intrinsic layer (i-layer) is considered the photoactive material. The electric field is modeled taking into account the built-in voltage V_{bi} given by the work function and/or doping of the layers on each side of the i-layer. Part of V_{bi} drops at the interfaces of the perovskite layer, leaving a reduced voltage $V_0 < V_{bi}$ for the intrinsic layer, which is approximated by the expression

$$V_0 = V_{bi} - 4V_t - 2V_t W\left(\frac{1}{2}\left(\frac{V_t d_{pvk}}{V_{bi} L_i}\right)^2 e^{\frac{V_{bi}}{2V_t}}\right),\tag{5}$$

where the symbol W represents the Lambert-W function, the thermal voltage $V_t = kT/q$ (being k Boltzmann's constant, T the absolute temperature, and q the elemental charge), L_i is the dielectric Debye-Hückel length of the intrinsic semiconductor given by $L_i = \sqrt{\varepsilon_r \varepsilon_0 V_t/(2qn_i)}$,[48] with ε_r the relative dielectric constant, ε_0 the permittivity of vacuum, and n_i the intrinsic carrier concentration. The remaining physical assumptions and parameters corresponding to the specific case of perovskite solar cells are detailed in Ref. [6]. The analytical current/voltage delivered by the drift-diffusion model using the electric field $(V - V_0)/d_{pvk}$ is given by[6]

$$J(V) = J_{dark}(V) - J_{ph}(V),\tag{6}$$

where J_{ph} is the photocurrent density given by

$$J_{ph}(V) = J_{ph,max} F_C(V),\tag{7}$$

where $J_{ph,max}$ is the maximum photocurrent and the voltage-dependent global collection efficiency F_C is given by

$$F_C(V) = 2\left(\frac{L}{d_{pvk}}\right)^2 \times \left\{(\beta_1 + \beta_2)\frac{1 + \left(\frac{\beta_1 - \beta_2 - Sd_{pvk}/D}{\beta_2 + Sd_{pvk}/D}\right)e^{-\beta_1/2}}{1 + \left(\frac{\beta_1 - Sd_{pvk}/D}{\beta_2 + Sd_{pvk}/D}\right)e^{-\frac{\beta_1 + \beta_2}{2}}} - \beta_1\right\}.\tag{8}$$

The effective diffusion constant D is obtained from the effective mobility μ from Einstein's relation $D = V_t\mu$, and the effective diffusion length is given by $L = \sqrt{D\tau}$. Here, β_1 and β_2 are dimensionless quantities given by

$$\beta_{1,2} = \sqrt{\left(\frac{d_{pvk}}{L}\right)^2 + \left(\frac{V - V_0}{2V_t}\right)^2} \pm \left(\frac{V - V_0}{2V_t}\right)\tag{9}$$

where the $\pm$ sign refers to β_1 and β_2, respectively. As seen from the above equations, the photocurrent depends on voltage through the voltage dependence of β_1 and β_2. At sufficiently low bias, Eq. (8) yields $F_C = 1$, resulting the maximum photocurrent.

The dark current density is given by

$$J_{dark}(V) = J_0(V) \times (e^{\frac{V}{2V_t}} - 1),\tag{10}$$

where J_0 is a voltage-dependent reverse saturation current density given by

$$J_0(V) = \frac{2qn_iD}{d_{pvk}} \times \left(\beta_1 + \frac{\beta_1 + \beta_2}{\left(\frac{Sd_{pvk}/D + \beta_2}{Sd_{pvk}/D - \beta_1}\right)e^{\frac{\beta_1 + \beta_2}{2}} - 1} \right). \quad (11)$$

Notice that in terms of a one–diode model,[14] the voltage-dependent terms contained in J_0 increase the slope of J_{dark}, which can be interpreted as an effective and voltage dependent ideality constrained between the values 1 and 2.

Keywords

[1] Y. Cheng, X. Xu, Y. Xie, H.-W. Li, J. Qing, C. Ma, C.-S. Lee, F. So, S.-W. Tsang, *Sol. RRL* **2017**, *1*, 1700097.

[2] U. Mehmood, A. Al-Ahmed, M. Afzaal, F. A. Al-Sulaiman, M. Daud, *Renew. Sust. Energ. Rev.* **2017**, *78*, 1.

[3] T. Leijtens, G. E. Eperon, A. J. Barker, G. Grancini, W. Zhang, J. M. Ball, A. R. Srimath Kandada, H. J. Snaith, A. Petrozza, *Energy Environ. Sci* **2016**, *9*, 3472.

[4] I. Grill, M. F. Aygüler, T. Bein, P. Docampo, N. F. Hartmann, M. Handloser, A. Hartschuh, *ACS Appl. Mater. Interfaces* **2017**, *9*, 37655.

[5] T. A. Berhe, W.-N. Su, C.-H. Chen, C.-J. Pan, J.-H. Cheng, H.-M. Chen, M.-C. Tsai, L.-Y. Chen, A. A. Dubale, B.-J. Hwang, *Energy Environ. Sci.* **2016**, *9*, 323.

[6] K. Taretto, M. Soldera, A. Koffman-Frischknecht, *IEEE J. Photovolt.* **2017**, *7*, 206.

[7] M. A. Green, Y. Hishikawa, W. Warta, E. D. Dunlop, D. H. Levi, J. Hohl-Ebinger, A. W. H. Ho-Baillie, *Prog. Photovolt. Res. Appl.* **2017**, *25*, 668.

[8] M. van Eerden, M. Jaysankar, A. Hadipour, T. Merckx, J. J. Schermer, T. Aernouts, J. Poortmans, U. W. Paetzold, *Adv. Opt. Mater.* **2018**, *5*, 1700151.

[9] J. M. Ball, S. D. Stranks, M. T. Hörantner, S. Hüttner, W. Zhang, E. J. W. Crossland, I. Ramirez, M. Riede, M. B. Johnston, R. H. Friend, H. J. Snaith, *Energy Environ. Sci.* **2015**, *8*, 602.

[10] R. Brendel, H. J. Queisser, *Sol. Energy Mater. Sol. Cells* **1993**, *29*, 397.

[11] P. Würfel, U. Würfel, *Physics of Solar Cells*, 3rd edn., Wiley, Weinheim, Germany **2016**.

[12] F. Staub, H. Hempel, J.-C. Hebig, J. Mock, U. W. Paetzold, U. Rau, T. Unold, T. Kirchartz, *Phys. Rev. Appl.* **2016**, *6*, 044017.

[13] Y. Yang, Y. Yan, M. Yang, S. Choi, K. Zhu, J. M. Luther, M. C. Beard, *Nat. Commun.* **2015**, *6*, 7961.

[14] K. Taretto, *Prog. Photovolt: Res. Appl.* **2014**, *22*, 870.

[15] A. Luque, S. Hegedus, *Handbook of Photovoltaic Science and Engineering*, 2nd edn., Wiley, West Sussex, United Kingdom **2011**.

[16] C. M. Wolff, F. Zu, A. Paulke, L. P. Toro, N. Koch, D. Neher, *Adv. Mater.* **2017**, *29*, 1700159.

[17] S. Chen, J. R. Manders, S.-W. Tsang, F. So, *J. Mater. Chem.* **2012**, *22*, 24202.

[18] D.A. Clugston, P.A. Basore, in Conference Record of the Twenty Sixth IEEE Photovoltaic Specialists Conference, (Ed. P.A. Basore), Institute of Electrical and Electronics Engineers, **1997**, 207.

[19] C.-W. Chen, S.-Y. Hsiao, C.-Y. Chen, H.-W. Kang, Z.-Y. Huang, H.-W. Lin, *J. Mater. Chem. A* **2015**, *3*, 9152.

[20] Q. Lin, A. Armin, R. C. R. Nagiri, P. L. Burn, P. Meredith, *Nat. Photon.* **2015**, *9*, 106.

[21] J.-P. Correa-Baena, M. Anaya, G. Lozano, W. Tress, K. Domanski, M. Saliba, T. Matsui, T. J. Jacobsson, M. E. Calvo, A. Abate, M. Grätzel, H. Míguez, A. Hagfeldt, *Adv. Mater.* **2016**, *28*, 5031.

[22] H. Zhou, Q. Chen, G. Li, S. Luo, T. Song, H.-S. Duan, Z. Hong, J. You, Y. Liu, Y. Yang, *Science* **2014**, *345*, 542.

[23] D. W. de Quilettes, S. M. Vorpahl, S. D. Stranks, H. Nagaoka, G. E. Eperon, M. E. Ziffer, H. J. Snaith, D. S. Ginger, *Science* **2015**, *348*, 683.

[24] N. D. Marco, H. Zhou, Q. Chen, P. Sun, Z. Liu, L. Meng, E.-P. Yao, Y. Liu, A. Schiffer, Y. Yang, *Nano Lett.* **2016**, *16*, 1009.

[25] T. Kirchartz, B. E. Pieters, K. Taretto, U. Rau, *Phys. Rev. B* **2009**, *80*, 035334.

[26] K. X. Steirer, P. F. Ndione, N. E. Widjonarko, M. T. Lloyd, J. Meyer, E. L. Ratcliff, A. Kahn, N. R. Armstrong, C. J. Curtis, D. S. Ginley, J. J. Berry, D. C. Olson, *Adv. Energy Mater.* **2011**, *1*, 813.

[27] K. M. McPeak, S. V. Jayanti, S. J. P. Kress, S. Meyer, S. Iotti, A. Rossinelli, D. J. Norris, *ACS Photonics* **2015**, *2*, 326.

[28] T. Kirchartz, F. Staub, U. Rau, *ACS Energy Lett.* **2016**, *1*, 731.

[29] COMSOL AB, RF Module User's Guide, **2008**.

[30] A.F. Lasagni, C. Gachot, K.E. Trinh, M. Hans, A. Rosenkranz, T. Roch, S. Eckhardt, T. Kunze, M. Bieda, D. Günther, V. Lang, F. Mücklich, in Proc. SPIE, Laser-based Micro- and Nano-processing XI, Vol. 10092, U. Klotzbach, K. Washio, R. Kling (Eds.), International Society For Optics And Photonics **2017**, 1009211.

[31] A. F. Lasagni, *Adv. Opt. Technol.* **2017**, *6*, 265.

[32] M. Sever, B. Lipovšek, J. Krč, A. Čampa, G. Sánchez Plaza, F.-J. Haug, M. Duchamp, W. Soppe, M. Topič, *Sol. Energy Mater. Sol. Cells* **2013**, *119*, 59.

[33] A. Campa, J. Krc, M. Topic, *Pr. Electromagn. Res.* **2013**, *137*, 187.

[34] K. Kang, S. Lee, J. Kim, S. Kim, Y. Han, S. Baek, *IEEE Photonics J.* **2016**, *8*, 1.

[35] M. Topič, M. Sever, B. Lipovšek, A. Čampa, J. Krč, *Sol. Energy Mater. Sol. Cells* **2015**, *135*, 57.

[36] J.-M. Jin, *The Finite Element Method in Electromagnetics*, 2nd edn., Wiley, New York, USA **2002**.

[37] L. A. A. Pettersson, L. S. Roman, O. Inganas, *J. Appl. Phys.* **1999**, *86*, 487.

[38] M. Soldera, K. Taretto, J. Berger, A. F. Lasagni, *Adv. Eng. Mater.* **2016**, *18*, 1674.

[39] M. Soldera, E. Estrada, K. Taretto, *Phys. Status Solidi A* **2013**, *210*, 1345.

[40] B. Shi, B. Liu, J. Luo, Y. Li, C. Zheng, X. Yao, L. Fan, J. Liang, Y. Ding, C. Wei, D. Zhang, Y. Zhao, X. Zhang, *Sol. Energy Mater. Sol. Cells* **2017**, *168*, 214.

[41] M. M. Tavakoli, Q. Lin, S.-F. Leung, G. C. Lui, H. Lu, L. Li, B. Xiang, Z. Fan, *Nanoscale* **2016**, *8*, 4276.

[42] L. Müller-Meskamp, Y. H. Kim, T. Roch, S. Hofmann, R. Scholz, S. Eckardt, K. Leo, A. F. Lasagni, *Adv. Mater.* **2012**, *24*, 906.

[43] Y. Park, J. Berger, P.-A. Will, M. Soldera, B. Glatz, L. Müller-Meskamp, K. Taretto, A. Fery, A.F. Lasagni, K. Vandewal, in Proc. SPIE Organic Photonics+ Electronics, Vol. 9942, Z.H. Kafafi, P.A. Lane, I.D.W. Samuel (Eds.) International Society For Optics And Photonics, **2016**, 994211.

[44] S. Ring, S. Neubert, C. Schultz, S. S. Schmidt, F. Ruske, B. Stannowski, F. Fink, R. Schlatmann, *Phys. Status Solidi-R* **2015**, *9*, 36.

[45] Z. Song, C. L. McElvany, A. B. Phillips, I. Celik, P. W. Krantz, S. C. Watthage, G. K. Liyanage, D. Apul, M. J. Heben, *Energy Environ. Sci.* **2017**, *10*, 1297.

[46] N. L. Chang, A. W. Yi Ho-Baillie, P. A. Basore, T. L. Young, R. Evans, R. J. Egan, *Prog. Photovolt: Res. Appl.* **2017**, *25*, 390.

[47] A.F. Lasagni, T. Roch, J. Berger, T. Kunze, V. Lang, E. Beyer, in Proc. SPIE, Laser-based Micro- and Nanoprocessing IX, Vol. 9351, U. Klotzbach, K. Washio, C. Arnold (Eds.), International Society For Optics And Photonics, **2015**, 935115.

[48] M. Sendner, P. K. Nayak, D. A. Egger, S. Beck, C. Müller, B. Epding, W. Kowalsky, L. Kronik, H. J. Snaith, A. Pucci, R. Lovrinčić, *Mater. Horiz.* **2016**, *3*, 613.